Journal of Geophysical Research
MAY 23 2007; 112 (C5) NIL_18-NIL_29
http://dx.doi.org/10.1029/2006JC003952

An edited version of this paper was published by AGU.

Tracking coherent structures in a regional ocean model with wavelet analysis: Application to Cape Basin eddies

A. M. Doglioli[1,*], B. Blanke[1], S. Speich[1], G. Lapeyre[3]

1 Laboratoire de Physique des Océans, UMR 6523 CNRS/IFREMER/UBO, Brest, France
2 Laboratoire de Météorologie Dynamique, ´ Ecole Normale Supérieure/IPSL, Paris, France

*: Corresponding author: doglioli@univmed.fr

Abstract:

This study is mainly aimed at proposing objective tools for the identification and tracking of three-dimensional eddy structures. It is conducted with a high-resolution numerical model of the ocean region around South Africa, and emphasis is put on Cape Basin anticyclones and cyclones thought to be actively implicated in the Indian-Atlantic interocean exchange. We settle on wavelet analysis for the decomposition and processing of successive maps of relative vorticity for a simulation run with ° resolution. The identification of three-dimensional coherent structures comes with the calculation of eddy trajectories and the time evolution of eddy properties. Instantaneous mass transport and momentum of eddies are calculated from the knowledge of instantaneous drift velocities, volumes, and diameters. The success of the regional model and of the analysis technique is assessed through comparisons with equivalent observations.

Keywords: Oceanic eddies; regional modeling; wavelet analysis; Agulhas current system; Southeast Atlantic ocean.

1. Introduction

The Agulhas Current is the most intense western boundary current of the World Ocean, and its retroflection shows one of the highest signals in eddy kinetic energy. Mesoscale eddies and large current rings pinch off from the Agulhas Retroflection and are usually associated with an Indian Ocean water leakage to the Atlantic Ocean [*Gordon*, 2003; *Richardson et al.*, 2003]. Satellite measurements in this area allow eddy tracking from sea surface height (SSH) anomalies [e.g., *van Ballegooyen et al.*, 1994; *Goñi et al.*, 1997; *Arhan et al.*, 1999]. Eddy trajectories can be reconstructed from successive surface elevation maps and coupled with in situ observations during concomitant cruises [e.g., *Garzoli and Goñi*, 2000]. As pointed out by *Morrow et al.* [2004], altimetry defines a robust way to track propagating features provided their typical scales are correctly sampled both in time and space by remote sensing. However, gaps in knowledge of the full three-dimensional (3D) identity of anticyclones and cyclones can obstruct more accurate diagnostics like the mass transport achieved by the eddy field. In this respect, numerical experiments are often fruitful. A primitive equation model of the Atlantic circulation allowed *Treguier et al.* [2003] to define Agulhas eddies from SSH anomalies with respect to a time mean. More recently, but for another oceanic region, *Penven et al.* [2005] developed an algorithm based on the calculation of the Okubo-Weiss parameter to systematize the process of eddy tracking in the Peru Current System. Indeed, *Okubo* [1970] and *Weiss* [1991] derived a criterion to separate flows into hyperbolic regions, where strain dominates, and elliptic ones where vorticity dominates. This criterion has been widely used to analyze numerical simulations of two-dimensional (2D) turbulence [*McWilliams*, 1984; *Elhmaidi et al.*, 1993, among others]. However, as pointed out by *Basdevant and Philipovitch* [1994], the validity of the criterion key assumption is restricted to the core of the vortices, i.e., the strongest elliptic regions of the flow. The Okubo-Weiss criterion is, therefore, not fully appropriate for a decomposition of a flow into background and eddy components.

The identification technique developed throughout this study is based on the wavelet analysis of modeled relative vorticity. Wavelets form an efficient basis set for localized structures such as ocean eddies. The main advantage of wavelets compared to Fourier transforms is that the former give information about a function or dataset with respect to scale and location in contrast to the latter, which provide a one-parameter family of coefficients representing the global frequency content. For the ocean, *Jameson and Miyama* [2000] applied wavelet analysis to the numerical resolution of Kelvin and Rossby waves. *Luo and Jameson* [2002] presented an application of wavelet analysis to time-evolving structures such as eddies and fronts described by numerical modeling or by satellite data. In fluid dynamics, both for numerical simulations and laboratory experiments [*Ruppert-Felsot et al.*, 2005; *Siegel and Weiss*, 1997, and references therein], the coherent and incoherent background components of a turbulent flow have been separated with a wavelet-based decomposition of the relative vorticity field. These successful applications drove us to apply the wavelet analysis technique used in 2D turbulence to the identification of eddies within horizontal slices of modeled relative vorticity. Then, in order to capture and track the full 3D envelope of each eddy, we developed an original and simple algorithm based on superimposing structures at different instants and different vertical levels.

Recently, *Boebel et al.* [2003] reviewed the theories proposed in the literature for the Indo-Atlantic interocean exchange. They limited the concept of "isolated Agulhas Rings embedded in a sluggish Benguela Drift" to the northwestern Cape Basin and called "Cape Cauldron" the southeastern Cape Basin, where mesoscale cyclone/anticyclone interactions result in vigorous stirring and mixing. This region is very appropriate as a field of study to test our technique with the aim to propose new clues to open questions about the role of oceanic mesoscale eddies. Our discussion is mainly devoted to four eddies, i.e. three anticyclones and one cyclone, obtained in a high-resolution numerical simulation of the ocean dynamics around Southern Africa. Section 2 describes the ocean model, whereas section 3 reports on the method we developed to identify 3D coherent structures and follow them as a function of time. In section 4, these structures are compared with those observed in the area under study, and then we introduce some parameters useful for eddy characterization. Our conclusions are drawn in section 5.

2. Ocean model

Our circulation model is based on the IRD (Institut de Recherche pour le Développement) version of the Regional Ocean Modeling System (ROMS). The reader is referred to *Shchepetkin and McWilliams* [2003, 2005] for a more complete description of the numerical code. The model domain extends from 10°W to 34°E and from 50°S to 25.4°S (Fig. 1). Its grid, forcing, initial and boundary conditions were built with the ROMSTOOLS package [*Penven*, 2003]. The model grid is 441×317 points with a resolution of $\frac{1}{10}^{\circ}$ corresponding to 9 km in mean grid spacing, which allows a correct sampling of the first baroclinic Rossby radius of deformation throughout the whole area (about 30 km according to *Chelton et al.* [1998]). The horizontal grid is isotropic with no introduction of asymmetry in the horizontal dissipation of turbulence. It therefore provides a fair representation of mesoscale dynamics. The model has 32 vertical levels, and the vertical s-coordinate is stretched for boundary layer resolution. The bottom topography is derived from a $2'$ resolution database [*Smith and Sandwell*, 1997]. Although a numerical scheme associated with a specific equation of state limits errors in the computation of the horizontal pressure gradient [*Shchepetkin and McWilliams*, 2003], the bathymetry field, h, must be filtered to keep the slope parameter, r, as $r = \frac{\nabla h}{2h} \leq 0.3$ [*Beckmann and Haidvogel*, 1993]. All the model external forcings are derived from climatologies. At the surface, the heat and fresh water fluxes introduced in the model are extracted from the Comprehensive Ocean-Atmosphere Data Set (COADS) [*Da Silva et al.*, 1994]. For the wind stress, a monthly mean climatology is computed from QuikSCAT satellite scatterometer data gridded at $\frac{1}{2}^{\circ}$ resolution [*Liu et al.*, 1998]. The contrast in resolution between the thermodynamical and dynamical atmospheric fields gives more weight to the dynamical forcing of the region [*Capet et al.*, 2004; *Blanke et al.*, 2005]. At the four lateral boundaries facing the open ocean, the model solution is connected to the surroundings by an active, implicit and upstream-biased radiation condition [*Marchesiello et al.*, 2001]. Under inflow conditions, the solution at the boundary is nudged toward temperature-, salinity- and geostrophic velocity-fields calculated from Levitus 1998 climatology (NODCWOA98 data provided by the NOAA/OAR/ESRL PSD, Boulder, Colorado, USA, from their Web site at http://www.cdc.noaa.gov/), which is also used for the initial state of the model. The geostrophic velocity is referenced to the 2000 dbar level. The width of the nudging border is 150 km, and the maximum viscosity value for the sponge layer is set to 1000 m^2s^{-1}.

We run an 11-year simulation with model outputs averaged and stored every 2 days of simulation. Fig. 2 shows the model-climatology of SSH and barotropic velocity obtained averaging these fields over the last 8 years of simulation. We find a fair agreement between simulated and observed circulation patterns [*Richardson et al.*, 2003, their Fig. 5]. A narrow and intense Agulhas Current flows along the eastern coast of Africa and eventually retroflects between 15°E and 20°E. In addition to the good reproduction of the meandering structure of the Agulhas Return Current, the simulation highlights the development of a high-level mesoscale activity characterized by the generation of Agulhas rings, anticyclones and cyclones, filaments and meanders (e.g., Fig. 3 and Fig. 4). The vigorous stirring and mixing processes observed by *Boebel et al.* [2003] in the so-called Cape Cauldron are well simulated. The model reproduces shear-edge cyclonic eddies in the bight of Agulhas Bank in good agreement with observed features [e.g. *Penven et al.*, 2001; *Lutjeharms et al.*, 2003]. Moreover, through a recent analysis of the same simulation, *Doglioli et al.* [2006] diagnosed an Indo-Atlantic interocean exchange of intensity comparable with the one inferred from observations.

3. Eddy identification and tracking

From the Wavelab library [http://www-stat.stanford.edu/~wavelab/] we developed a set of MATLAB routines to analyze the circulation calculated by the ocean model. Our procedure can be decomposed into three steps: wavelet analysis, time tracking and vertical tracking.

3.1. Wavelet Analysis

The wavelet analysis consists in the decomposition of a signal under study into orthogonal, multi-resolution wavepackets in a way similar to a Fourier decomposition. Such a technique allows efficient data compression of various signals such as images or sounds. A wavepacket is a square integrable modulated waveform well-localized in both position and wavenumber. Since such a method was applied in the past to the extraction of eddies in 2D turbulence [*Siegel and Weiss*, 1997], the reader is referred to this paper for a thorough discussion about the pertinence and details of the wavelet transform. Here, the wavepackets are used to decompose successive horizontal maps of relative vorticity and to extract localized structures in space. We also choose the Haar basis, which is an orthonormal basis of $L^2(R^2)$ [*Daubechies*, 1988, 1992]. The algorithm in use has four different sub-steps: at first, a best basis is found to minimize a cost function (here, the Shannon entropy) [*Wickerhauser*, 1994; *Coifman and Wickerhauser*, 1992]; this basis varies with each time step under consideration and allows one to find the best location for the wavepackets. Second, the model relative vorticity is expanded on this basis. Third, the wavelets are sorted out as a function of their wavelet coefficients. Only the wavelets with the largest coefficients are kept. The number of coefficients that are kept depends on the dimension of the basis computed using the Shannon entropy (usually 10% of the initial set of wavelets). The method acts as pattern recognition since the reconstructed signal is zero wherever there is no identified pattern. Four, the structures are extracted one after the other by searching, first, the maximum of the vorticity modulus, then by spreading the structure in each direction in space till finding a minimum in vorticity. At last we merge together adjacent structures with more than 6 gridcell edges in common, and we eliminate filamentary patterns by ignoring structures less than 4-gridpoint wide. The resulting localized structures that cover more than 30 model gridcells, i.e., roughly 2500 km^2, are kept and used to separate and define eddies.

Processing relative vorticity with a wavelet-based decomposition gives excellent results in terms of eddy identification (as already shown by *Ruppert-Felsot et al.* [2005]). Relative vorticity tends to overemphasize frontal structures since it intensifies with the vertical motions that develop in oceanic fronts [*Wang*, 1993]. This quantity is, therefore, suitable for eddy edge detection. It also reveals small-scale filaments that can be easily removed because of their elongated shape and small coverage area. Moreover, relative vorticity is free from large-scale gradients unlike Ertel potential vorticity, which incorporates the β effect and is sensitive to large-scale spatial density gradients. Equivalent gradients are also present in temperature, salinity and SSH. On the other hand, the use of relative vorticity does not require the somewhat arbitrary definition of a reference field to calculate anomalies. Lastly, the Okubo-Weiss parameter lies on an assumption that restricts eddy detection to eddy cores [*Basdevant and Philipovitch*, 1994]. Its use would prevent an efficient decomposition between background and eddy signals.

We performed several tests to optimize the parameters involved in the first step of our analysis. It turns out that the critical parameter is the number of spectral coefficients kept for signal reconstruction. Our best results are obtained with a percentage of about 9 to 11%. Fig. 3 shows an example of results issued from our analysis. The 256×256-gridpoint domain spans the region to the northwest of the Agulhas retroflection. The relative vorticity map (Fig. 3a) is calculated at -200 m on day 11 / month 3 / year 7. Among the 44 identified structures, some patterns look like filaments or meanders, but most of them are well-defined eddies. The following discussion will focus on (i) the cyclone at 33°S, 9°E (letter P, hereafter referred to as Panoramix), (ii) the anticyclone at 30°S, 10°E (letter I, hereafter referred to as Idefix), (iii) the anticyclone at 32°S, 5°E (letter O, hereafter referred to as Obelix) and (iv) the anticyclone at 36°S, 4°E (letter A, hereafter referred to as Asterix). The eddy signal is also clearly present in SSH (Fig. 3b). The wavelet-based eddy contours fit well with the negative anomaly induced by cyclone Panoramix (contour -0.1 m) and with the positive anomalies of anticyclones Idefix, Obelix and Asterix (contours +0.3, +0.4 and +0.5 m, respectively). SSH captures only the large-scale patterns of the eddy field because it is related to the baroclinic streamfunction characterized by weak gradients at the eddy periphery. Patterns in temperature (Fig. 3c) and salinity (Fig. 3d) at depth 200 m are also in good agreement with the wavelet analysis for the cyclone (colder and fresher than surrounding water) and anticyclones (warmer and saltier). This is true for most of the eddies except for some discrepancies likely due to the presence of a large-scale salinity and temperature gradient superimposed on the eddy signature. A better eddy identification based on temperature or salinity fields would require the removal of a mean climatological component. The comparison of the wavelet analysis with the Ertel potential vorticity at -200 m (Fig. 3e) confirms that our technique is able to correctly detect the whole eddy area. Identified cyclones (anticyclones) precisely overlap with the contours of 7 (5)$\times 10^{-10}$ $m^{-1}s^{-1}$. The Okubo-Weiss criterion was also tested for comparison (Fig. 3f). In this field, the cores of the vortices correspond to the strongest elliptic regions (where vorticity dominates strain) and are characterized by strongly negative values of the parameter. However, our analysis is somewhat better since it gives eddy contours close to the structure shown by the Ertel potential vorticity. The Okubo-Weiss criterion characterizes only the inner core of the eddies.

At the end of this step, each identified structure is numbered, and its area, A, is measured. The eddy center is defined as the gridpoint of local maximum of absolute relative vorticity over the eddy area, A, with a precision corresponding to the model grid spacing. Let us define the diameter, D, as the average of the zonal (D^{EW}) and meridional (D^{NS}) cords that intercept each eddy center with both endpoints on the edge of the structure (defined through the wavelet analysis). This definition accounts for stretched shapes.

3.2. Time tracking

Tracking identified eddies forward in time requires that the following criterion be satisfied:

$$c_{t,z=-200} \in \mathfrak{E}_{t-\Delta t,z=-200} \tag{1}$$

where $c_{t,z=-200} \equiv (ic, jc)_{t,z=-200}$ is the eddy center at the time, t, and depth -200 m and $\mathfrak{E}_{t-\Delta t}$ is the set of gridpoints of the same eddy at the previous time step. The sampling period of the model output, $\Delta t = 2$ days, was proven by several tests to cause no bias in the analysis (data not shown). The translational velocity of the eddy is calculated as the distance covered by the eddy center over successive 2-day intervals. At each time step of the analysis, the instantaneous translational velocity, v, and the diameter, D, of each coherent eddy are both recorded. As criterion (1) can be easily adapted for backward time tracking, we checked that both tracking directions led to very comparable results. Thus, an eddy identified at a specific instant is tracked both backward and forward in time until criterion (1) cannot be satisfied, which stops the analysis. The last instants of the forward and backward trackings are considered as the "death" and "birth" of the eddy, respectively. Fig. 4 shows eddy contours and surrounding relative vorticity at the end of Panoramix and Idefix time trackings. Cyclone Panoramix stops when it becomes an elongated filament of negative vorticity (Fig. 4a1), whereas its backward time tracking shows its formation on the continental slope near Cape Columbine (Fig. 4a2). Anticyclone Idefix is followed forward in time until it merges with a larger anticyclone to the north of Walvis Ridge (Fig. 4b1) and backward in time till it detaches itself from a large anticyclonic structure under pressure from a cyclone moving southwestward (Fig. 4b2).

3.3. Vertical tracking

The analysis is repeated at several depths to diagnose the vertical extent of an eddy identified at first at -200 m. The analysis is started at this depth to eliminate the model surface layers liable to be affected by a dynamics too much sensitive to air-sea interactions. Let us state that a structure identified at the level, z, belongs to an eddy already identified at the level, $z - \Delta z$, on condition to satisfy criterion (2):

$$c_z \in \mathfrak{E}_{z-\Delta z} \tag{2}$$

where $c_z \equiv (ic, jc)_z$ is the center of the structure identified at the level, z, and $\mathfrak{E}_{z-\Delta z}$ is the set of gridpoints of the selected eddy at the level, $z - \Delta z$. After sensitivity tests and computing time considerations, we set the distance between two successive horizontal slices to $\Delta z = 100$ m. The vertical tracking ends at depth iz_L just before the eddy signal in relative vorticity becomes too weak to be detected. In order to avoid an excessive vertical extent of eddies, our vertical tracking was stopped at $z_{max} = -1000$ m (see Fig. 5). This maximum depth matches the vertical extent of Agulhas rings that are usually found in field measurements [*Garzoli et al.*, 1999; *Schmid et al.*, 2003] and numerical models [*Donners et al.*, 2004].

We also checked that the vertical extent found for the eddies was in agreement with a maximum depth based on the *Flierl* [1981] criterion. It is worth noting that, with this criterion, an eddy can be tracked with depth as long as its rotational speed exceeds its translation speed. We calculated the rotational speed of our eddies by averaging the tangential velocity at the ends of both diameters D^{EW} and D^{NS}, and we defined their translation speed, v, as in section 3.2. After computation of the deepest immersion at which *Flierl* [1981] criterion could be satisfied (hereafter z_{Flierl}), this parameter was considered as undefined when it approached the local ocean floor by less than 1000 m. Fig. 5 exhibits smooth evolutions of z_{Flierl} and iz_L for cyclone Panoramix (upper panel) and anticyclone Idefix (bottom panel) except on the occasion of sudden deepenings for brief periods. These events happen mostly when the translational velocity of the eddy decreases, and the upper 1000 m of the structure are able to spin up movements in the layers underneath. Indeed, *van Aken et al.* [2003] showed that an Agulhas ring rotating with relatively intense kinetic energy can extend down to the ocean bottom. In our simulation, we observed good correlation of z_{Flierl} and iz_L with the translational velocity, v, of the eddy, and to stop vertical tracking at $z_{max} = -1000$ m when z_{Flierl} reaches deepest values seems realistic. Then, for cyclone Panoramix (Fig. 5a), the Flierl criterion confirms that the eddy extends at least down to 1000m for quite some time (from 5 to day 60). The vertical extension of anticyclone Idefix is smaller (Fig. 5b) and both definitions of its maximum depth give equivalent results.

In summary, at a fixed time step, the area, A_k, and diameter, D_k, are both diagnosed at each level, k, and the volume, V, taken up by each eddy can be calculated as:

$$V = \sum_{k=1}^{iz_L} A_k \cdot \Delta z. \quad (3)$$

The knowledge of instantaneous velocity v, diameter D and volume V of each structure enables one to calculate an instantaneous transport and an instantaneous momentum denoted $Tinst$ and $Minst$ respectively (see Appendix A and section 4).

4. Results and discussion

Let us, now, focus on the three anticyclones, Asterix, Idefix and Obelix, and the cyclone, Panoramix, successfully tracked by our technique between the end of year 6 and the end of year 7 of our 11-year simulation. In slightly more than 6 months (day 10 / month 11 / year 6 to 14/5/7, in southern summer and fall) Panoramix moved mainly west-southwestward and eventually turned south just before turning into a filament (Fig. 1 and Fig. 4a). Tracking of Idefix for slightly less than 10 months, from 3/12/6 to 11/10/7 (in southern summer, fall and winter) highlighted a northwestward motion (Fig. 1 and Fig. 4b). Obelix (from 10/11/6 to 5/3/7) and Asterix (from 14/1/7 to 13/6/7) also moved along this direction (Fig. 1). Such a divergence in eddy pathways between cyclones and anticyclones has been also reported from satellite- and drifter-data [*Boebel et al.*, 2003; *Morrow et al.*, 2004]. According to *Morrow et al.* [2004], it is induced by changes in planetary and relative vorticity on the flanks of the eddy, but other causes are possible.

The time series for cyclone Panoramix (Fig. 6 and Appendix A for details on the calculation of the associated error bars) show different periods in the life of the eddy. When the eddy moves over the continental slope, its translational velocity is weak, and its shape is more or less circular. Indeed, there is nearly no change in diameter and volume during this first stage. Then, the cyclone moves into the Cape Basin and starts to interact with other eddies and filaments. Before it becomes itself a filament, the successive growth and reduction of its volume as well as a high variability of its diameter indicate that it incorporates and loses some mass. Its instantaneous transport and momentum are increasing both in magnitude and variability during this stage.

Among the time series obtained for the three anticyclones, the Idefix one is the longest (Fig. 7). Velocity, volume and diameter show significant variability at the stage of eddy formation. Then, there is a central period over which the eddy is well structured, and its volume and diameter remain nearly unchanged as it is moving within the Cape Basin. These small variations indicate that our algorithm works fairly well for eddy identification: the eddies that do not interact with their surroundings should indeed conserve their tracer properties in time. The variation in volume and velocity between 170 and 210 days of its lifetime is caused by the crossing of the Walvis Ridge (Fig. 5b). Beyond the ridge, the eddy volume is reduced and the velocity is less regular. Here, large standard deviations in diameter with no correspondence with large standard deviations in volume are the sign of a shape becoming more and more stretched. The instantaneous transport and momentum show a general decline over the eddy lifetime, suggesting a loss of impetus during its northwestward journey, whereas modulations in time look mainly driven by velocity changes.

Table 1 summarizes the time-averaged values of eddy parameters. The cyclone, Panoramix, and the anticyclone, Idefix, have similar translational velocities, whereas the other two anticyclones are moving faster. The difference may partly come from the shortness of the tracking of Obelix and Asterix since a short time series likely induces a bias on the calculation of average values. A comparison with previous studies suggests that our estimates of drift velocity, volume and diameter for Cape Basin eddies are realistic. Cyclones and anticyclones tracked by *van Ballegooyen et al.* [1994] had drift velocities between 0.037 ms^{-1} and 0.090 ms^{-1}. In *Arhan et al.* [1999], the anticyclone, R3, displays a path very close to the one we obtain for Idefix, with a mean drift velocity of 0.09 ms^{-1} (when averaged over 100 days). Similar values were found by *Garzoli et al.* [1999] who pointed out that such velocities fall within the range of previous observations [*Goñi et al.*, 1997]. More recently, *Schmid et al.* [2003] observed and tracked a specific Agulhas Ring with satellite altimetry and RAFOS trajectories; the translational velocity estimated by altimetry ranged from 0.011 to 0.273 ms^{-1} (with an estimated error of about 0.03 ms^{-1}). For some periods, these authors also found a match between drift estimates calculated from RAFOS floats and averaged values calculated from altimetry. *van Aken et al.* [2003] calculated drift velocities of about 0.03 and 0.10 ms^{-1} for two different rings. Observations reported by *Boebel et al.* [2003] and *Morrow et al.* [2004] showed a faster motion of anticyclones compared with cyclones. Our results agree with this statement, but our modeled drift velocities are about twice their estimates. In a model of the Atlantic circulation, *Treguier et al.* [2003] calculated the average velocity of Agulhas Rings once they had crossed Walvis Ridge, and pointed out that their result (0.06 ms^{-1}) was similar to velocities diagnosed by *Schouten et al.* [2000] and *Garnier et al.* [2003] from altimetry data.

As regards volume and diameter, our anticyclones are in average smaller than observed Agulhas rings [*van Aken et al.*, 2003, and references cited therein]. This bias is mainly attributable to the nature of the comparison. Estimates cited in literature often correspond to instantaneous or short-term averaged values, whereas our mean parameters were calculated over several months of tracking. Our recorded maximum values (omitting error bars) of V=23, 31 and 33 10^{12} m^3 and D=195, 273 and 219 km for Idefix, Obelix and Asterix, respectively, are in fact in fair agreement with typical observations at sea. Furthermore, our definition of eddy volume is not based on hydrological criteria as done in most previous studies (e.g., the water volume above the 10°C isotherm), and our definitions of diameter and area apply also to non-circular eddies. Planned analyses of hydrological properties of modeled eddies will address a more accurate comparison with observations. Nevertheless, we already point out that our estimate of the ratio between diameter and volume is in good agreement with the one found for observed eddies. Our conclusions also hold for cyclones though the data available in the literature about this topic in the Cape Basin are far less numerous. *Boebel et al.* [2003] found a typical diameter of 120 km for these structures, whereas *van Ballegooyen et al.* [1994] measured an initial dimension of 160 km for a cyclone formed near the Agulhas retroflection.

Besides translational velocity, volume and diameter, we suggest two other physical quantities that we consider to be meaningful for differentiating individual contributions to transport by coherent eddies: the instantaneous transport, $Tinst$, and the instantaneous momentum, $Minst$ (see Appendix A for mathematical definitions). $Tinst$ represents the instantaneous transport induced by an eddy of a given volume crossing completely a fixed imaginary section positioned in front of it, i.e., covering a distance equal to its diameter while moving at its drift velocity. $Minst$ accounts directly for the momentum of the eddy and is obtained by multiplying its mass by its velocity. Our definition for transport differs from the one generally used in data analysis [e.g., *van Ballegooyen et al.*, 1994] or models [*Treguier et al.*, 2003]. The "classical" approach calculates the individual transport by dividing the typical volume of an eddy by 1 yr. Multiplying this transport by the average number of equivalent propagating structures per year gives an estimate of the mean transport achieved by the eddy field and can be used, for instance, to diagnose the transmission of water from the Indian to the Atlantic Ocean in the form of coherent eddies. This definition would lead to transport values of about 0.4 Sv for Obelix and Asterix. On the contrary, as our definition of instantaneous transport does not lie on the arbitrary definition of a reference time interval, it is appropriate for the intercomparison of individual structures because of the involvement of three main characteristics of an eddy (velocity, shape and volume). The application of our definition to specific eddies with available data about drift velocity, volume and diameter [e.g. *van Ballegooyen et al.*, 1994; *van Aken et al.*, 2003; *Schmid et al.*, 2003] leads to values for $Tinst$ of the same order of magnitude as our modeled eddies.

5. Summary and conclusions

The main goal of our study was to propose objective tools for identification and tracking of 3D coherent structures. Wavelet analysis allowed us to follow eddies in space and time as long as they exist as coherent structures in the model and to evaluate their translational velocity, diameter, volume and derived parameters.

This study was carried out in a regional ocean model that accounts for eddy displacements within the Cape Basin region. This oceanic region around Southern Africa is a critical water mass crossroads within the so-called warm-water route of the global overturning circulation [*Gordon*, 1986; *Gordon et al.*, 1992; *Gordon*, 2003]. Oceanic eddies are of key importance in the distribution of properties like heat and salt throughout the World Ocean, and Agulhas rings are thought to play a key role in the Indo-Atlantic interocean exchange [*Gordon*, 1986; *de Ruijter et al.*, 1999; *Weijer et al.*, 1999]. The Indo-Atlantic connection appears crucial in global ocean models too [*Speich et al.*, 2001, 2002]. Furthermore, recent studies based on observations found a highly nonlinear regime in the Cape Basin (the first Atlantic basin to collect leakage of Agulhas water) [*Boebel et al.*, 2003]. Turbulence is so intense in this area that it could prevent the continuous advection of Indian or South Atlantic waters [*de Ruijter et al.*, 1999]. Indeed, in the Cape Basin, eddies of different types interact with each other and with the main retroflection of the Agulhas Current, in a context of vigorous stirring and mixing [*Gordon*, 2003; *Boebel et al.*, 2003; *Morrow et al.*, 2004].

In this turbulent framework, we processed maps of modeled relative vorticity with a wavelet-based decomposition. Then, in order to capture and track the full 3D envelope of each eddy, we developed an algorithm based on superimposing structures at different instants and different vertical levels. The brief presentation of our validation dealt with only a few of the numerous mesoscale structures simulated by the model. Indeed, we decided to focus mostly on two types of mesoscale vortices, i.e. i) cyclonic eddies ejected into the open ocean from the Southwestern African continental slope and ii) anticyclonic eddies present in the Cape Basin. Our tracking evidenced divergent pathways for both types with a westward and equatorward propagation at a speed within 0.08 and 0.13 ms^{-1} for anticyclones and a westward, but poleward propagation at 0.08 ms^{-1} for the studied cyclone. Both behaviors are very similar to those observed with altimetry along different subtropical eastern boundaries [*Morrow et al.*, 2004]. Our translational velocities are slightly larger than those derived from altimetry and RAFOS floats, but the tracking criteria were not alike [*van Ballegooyen et al.*, 1994; *Boebel et al.*, 2003; *Morrow et al.*, 2004]. Diameter and volume timeseries obtained with our analysis provide useful information on the evolution of the shape of an eddy and on the interactions with surrounding structures. Time-averaged diameters range from 81 to 156 km with instantaneous values exceeding 200 km and time-averaged volumes range from 4 to 14 10^{12} m^3 with instantaneous values exceeding 30 10^{12} m^3, in good agreement with observational data [*van Aken et al.*, 2003, and references cited therein]. Analyses of hydrological properties of modeled eddies will be necessary for a more thorough comparison. Then, besides translational velocity, volume and diameter, we suggest the calculation of two derived parameters that prove appropriate for the intercomparison of individual structures: the instantaneous transport and the instantaneous momentum.

Tracking techniques based on the calculation of Lagrangian trajectories also exist, as shown for instance by a recent analysis of the same numerical simulation [*Doglioli et al.*, 2006]. Such Lagrangian computations coupled with the wavelet-based definition of each eddy volume will be used in a future paper to calculate the remote origins and fates of the water carried by each structure. Heat and fresh water transport estimates will also be derived for each type of eddy. This will allow the evaluation (in models) of the relevance of the ocean off South Africa in the organization of the return branch of the global thermohaline circulation. We plan to evaluate accurately the net exchanges across the Cape Basin in order to gain more insight into the complex role of the mesoscale processes affecting the origin and fate of water masses.

Acknowledgments.

The authors wish to thank Michel Arhan, Xavier Carton, Steven Herbette, Guillaume Roullet and Anne-Marie Treguier for enlightening discussions about eddy dynamics, and Marie-Paule Friocourt for her assistance in correcting the manuscript. A. M. Doglioli is supported by SHOM, under contract number CA 2003/03/CMO (Contact: Alain Serpette). This study is also a contribution to InterUp, a project funded by the French LEFE-IDAO program (Les Enveloppes Fluides et l'Environnement - Interactions et Dynamique de l'Océan et de l'Atmosphère), formerly PATOM (Programme National Atmosphère et Océan à Multi-échelles).

Appendix A: Definitions

Let us define the instantaneous mass transport of a coherent eddy as the ratio between the eddy volume, V, and the time, Δt, needed to cross entirely a fixed section perpendicular to the direction of propagation of the eddy center:

$$Tinst = V \cdot \Delta t^{-1}. \tag{A1}$$

Assuming that the time interval is $\Delta t = D \cdot v^{-1}$ where D is the eddy diameter and v is the velocity of the eddy center, the transport is estimated as:

$$Tinst = v \cdot V \cdot D^{-1}. \tag{A2}$$

In our calculations,

$$v \equiv v(t) = \frac{1}{iz_L} \sum_{k=1}^{iz_L} v_k$$

is the vertical average of the velocity of the eddy center as computed for each z-layer with a backward difference scheme involving successive positions. The relative error $v_{err} \equiv v_{err}(t)$

made on velocity is estimated as:

$$v_{err} = \frac{\sigma_z(v)}{v}, \quad \text{(A3)}$$

where σ_z is the standard deviation of the distribution along the vertical axis.

As described above, our analysis gives the eddy volume at each time step. Our estimate of the relative error $V_{err} \equiv V_{err}(t)$ on the volume calculation is

$$V_{err}(t) = \frac{\Delta z \pi \left(\frac{D}{2}\right)^2}{V} + \frac{4 \Delta x \Delta z \sum_{k=1}^{iz_L} A_k D_k^{-1}}{V}, \quad \text{(A4)}$$

that is the sum of errors due to the vertical (step Δz) and horizontal (step Δx) discrete representations of the eddy. The first term on the right-hand side is the volume of the cylinder that the method may neglect at the base of the eddy. The second term is the approximate volume of a cylindrical ring neglected or taken by mistake around the eddy whose area, A_k, and diameter, D_k, are diagnosed at each level, k.

Let us define the diameter, D, as the mean between the zonal (D^{EW}) and the meridional (D^{NS}) cords that intercept each eddy center with both endpoints on the edge of the structure. Then, by repeating this average at each level, k, the reference diameter used in A2 is:

$$D = \frac{1}{2\, iz_L} \sum_{k=1}^{iz_L} \left(D_k^{EW} + D_k^{NS} \right). \quad \text{(A5)}$$

For stretched eddies in rotation, the relative error made on the calculation of D with A5 is estimated as:

$$D_{err} = \frac{1}{iz_L} \frac{\sum_{k=1}^{iz_L} \left| D_k^{EW} - D_k^{NS} \right|}{D}. \quad \text{(A6)}$$

The relative error on our transport estimate is the sum of the errors defined in A3, A4 and A6:

$$Tinst_{err} = v_{err} + V_{err} + D_{err}.$$

The mean transport, $\overline{Tinst}$, is the time average of $Tinst$. Equivalently, we introduce the instantaneous momentum (and associated error) of a coherent structure as the product of its instantaneous velocity and volume. Ignoring density variations within the structure and thus using $\rho_0 = 1020 kg/m^3$ lead to:

$$Minst = \rho_0 \cdot V \cdot v,$$

and

$$Minst_{err} = v_{err} + V_{err}.$$

Finally, the mean momentum, $\overline{Minst}$, is the time average of $Minst$.

References

Arhan, M., H. Mercier, and J. R. Lutjeharms (1999), The disparate evolution of three Agulhas rings in the South Atlantic Ocean, *J. Geophys. Res.*, *104*(C9), 20 987–21 005.

Basdevant, C., and T. Philipovitch (1994), On the validity of the "Weiss criterion" in two-dimensional turbulence, *Physica D*, *113*, 17–30.

Beckmann, A., and D. Haidvogel (1993), Numerical simulation of flow around a tall isolated seamount. Part 1: Problem formulation and model accuracy, *J. Phys. Oceanogr.*, *23(8)*, 1736–1753.

Blanke, B., S. Speich, A. Bentamy, C. Roy, and B. Sow (2005), Modeling the structure and variability of the southern Benguela upwelling using QuikSCAT wind forcing, *J. Geophys. Res.*, *110*, C07018, doi:10.1029/2004JC002529.

Boebel, O., J. Lutjeharms, C. Schmid, W. Zenk, T. Rossby, and C. Barron (2003), The cape cauldron: a regime of turbulent inter-ocean exchange, *Deep-Sea Res. II*, *50*, 57–86.

Capet, X., P. Marchesiello, and J. McWilliams (2004), Upwelling response to coastal wind profiles, *Geophys. Res. Lett.*, *31*, L13311, doi:10.1029/2004GL020123.

Chelton, D. B., R. A. deSzoeke, M. G. Schlax, K. El Naggar, and N. Siwertz (1998), Geographical variability of the first-baroclinic Rossby radius of deformation, *J. Phys. Oceanogr.*, *28*, 433–460.

Coifman, R. R., and M. V. Wickerhauser (1992), Entropy based algorithms for best basis selection, *IEEE Trans. on Inf. Theory*, *32*, 712–718.

Da Silva, A. M., C. C. Young, and S. Levitus (1994), Atlas of surface marine data 1994, vol. 1, algorithms and procedures, *Tech. rep.*, U. S. Department of Commerce, NOAA.

Daubechies, I. (1988), Orthonormal basis of compactly supported wavelets, *Commun. Pure Appl. Math.*, pp. 909–996.

Daubechies, I. (1992), *Ten Lectures on Wavelets*, 357 pp., Society for Industrial and Applied Mathematics.

de Ruijter, W. P. M., A. Biastoch, S. S. Drijfhout, J. R. E. Lutjeharms, R. P. Matano, T. Pichevin, P. J. van Leeuwen, and W. Weijer (1999), Indian-Atlantic interocean exchange: Dynamics, estimation and impact, *J. Geophys. Res.*, *104*(C9), 20 885–20 910.

Doglioli, A. M., M. Veneziani, B. Blanke, S. Speich, and A. Griffa (2006), A Lagrangian analysis of the Indian-Atlantic interocean exchange in a regional model, *Geophys. Res. Lett.*, *33*, L14611, doi:10.1029/2006GL026498.

Donners, J., S. S. Drijfhout, and A. Coward (2004), Impact of cooling on the water mass exchange of Agulhas rings in a high resolution ocean model, *Geophys. Res. Lett.*, *31*, L16312, doi:10.1029/2004GL020644.

Elhmaidi, D., A. Provenzale, and A. Babiano (1993), Elementary topology of two-dimensional turbulence from a Lagrangian viewpoint and single-particle, *J. Fluid Mech.*, *257*, 533–558.

Flierl, G. R. (1981), Particle motions in large-amplitude wave fields, *Geophys. Astrophys. Fluid Dyn.*, *18*, 39–74.

Garnier, E., J. Verron, and B. Barnier (2003), Variability of the South Atlantic upper ocean circulation: a data assimilation experiment with 5 years of TOPEX/POSEIDON altimeter observations, *International Journal of Remote Sensing*, *24*(5), 911–934.

Garzoli, S. L., and G. J. Goñi (2000), Combining altimeter observations and oceanographic data for ocean circulation and climate studies, in *Satellite, Oceanography and Society*, edited by D. Halpern, chap. 5, pp. 79–97, Elsevier Science B.V.

Garzoli, S. L., P. L. Richardson, C. D. Rae, D. M. Fratantoni, G. J. Goñi, and A. J. Roubicek (1999), Three Agulhas rings observed during the Benguela Current Experiment, *J. Geophys. Res.*, *104*(C9), 20 971–20 985.

Goñi, G. J., S. L. Garzoli, A. J. Roubicek, D. B. Olson, and O. B. Brown (1997), Agulhas ring dynamics from TOPEX/POSEIDON satellite altimeter data, *J. Mar. Res.*, *55*, 861–883.

Gordon, A. L. (1986), Interocean exchange of thermocline water, *J. Geophys. Res.*, *91*, 5037–5046.

Gordon, A. L. (2003), The brawniest retroflection, *Nature*, *421*(6926), 904–905.

Gordon, A. L., R. F. Weiss, W. M. Smethie, and M. J. Warner (1992), Thermocline and Intermediate Water Communication between the South-Atlantic and Indian Oceans, *J. Geophys. Res.*, *97*, 7223–7240.

Jameson, L., and T. Miyama (2000), Wavelet analysis and ocean modeling: A dynamically adaptive numerical method “WOFD-AHO”, *Mon. Wea. Rev.*, *128*, 1536–1548.

Liu, W. T., W. Tang, and P. S. Polito (1998), NASA scatterometer provides global ocean-surface wind fields with more structures than numerical weather prediction, *Geophys. Res. Lett.*, *25*(6), 761–764, doi:10.1029/98GL00544.

Luo, J., and L. Jameson (2002), A wavelet-based technique for identifying, labeling, and tracking of ocean eddies, *J. Atmos. Ocean. Technol.*, *19*(3), 381–390.

Lutjeharms, J. R. E., O. Boebel, and H. T. Rossby (2003), Agulhas cyclones, *Deep-Sea Res. II*, *50*, 13–34.

Marchesiello, P., M. J. C., and A. Shchepetkin (2001), Open boundary condition for long-term integration of regional oceanic models, *Ocean Model.*, *3*, 1–21.

McWilliams, J. C. (1984), The emergence of isolated coherent vortices in turbulent flow, *J. Fluid Mech.*, *146*, 21–43.

Morrow, R., F. Birol, D. Griffin, and J. Sudre (2004), Divergent pathways of cyclonic and anti-cyclonic ocean eddies, *Geophys. Res. Lett.*, *31*, L24311, doi:10.1029/2004GL020974.

Okubo, A. (1970), Horizontal dispersion of floatable particles in the vicinity of velocity singularities such as convergences, *Deep-Sea Res.*, *17*, 445–454.

Penven, P. (2003), ROMSTOOLS user guide, *Tech. rep.*, Inst. de Rech. pour le Dév., Paris, France, http://www.brest.ird.fr/Roms_tools.

Penven, P., J. R. E. Lutjeharms, P. Marchesiello, C. Roy, and S. J. Weeks (2001), Generation of cyclonic eddies by the Agulhas Current in the lee of the Agulhas Bank, *Geophys. Res. Lett.*, *27*(6), 1055–1058.

Penven, P., V. Echevin, J. Pasapera, F. Colas, and J. Tam (2005), Average circulation, seasonal cycle, and mesoscale dynamics of the Peru Current System: A modeling approach, *J. Geophys. Res.*, *110*, C10021, doi:10.1029/2005JC002945.

Richardson, P. L., J. R. E. Lutjeharms, and O. Boebel (2003), Introduction to the "Inter-ocean exchange around southern Africa", *Deep-Sea Res. II*, *50*, 1–12.

Ruppert-Felsot, J. E., O. Praud, E. Sharon, and H. L. Swinney (2005), Extraction of coherent structures in a rotating turbulent flow experiment, *Phys. Rev. E*, *72*(016311).

Schmid, C., O. Boebel, W. Zenk, J. R. E. Lutjeharms, S. L. Garzoli, P. L. Richardson, and C. Barron (2003), Early evolution of an Agulhas Ring, *Deep-Sea Res. II*, *50*(1), 141–166.

Schouten, M., W. de Ruijter, and P. van Leeuwen (2000), Translation, decay and splitting of Agulhas rings in the southeastern Atlantic Ocean, *J. Geophys. Res.*, *105*, 21 913–21 925.

Shchepetkin, A. F., and J. C. McWilliams (2003), A method for computing horizontal pressure-gradient force in an oceanic model with nonaligned vertical coordinate, *J. Geophys. Res.*, *108*(C3), 3090, doi:10.1029/2001JC001047.

Shchepetkin, A. F., and J. C. McWilliams (2005), The regional oceanic modeling system (ROMS): a split-explicit, free-surface, topography-following-coordinate oceanic model, *Ocean Model.*, *9*, 347–304.

Siegel, A., and J. B. Weiss (1997), A wavelet-packet census algorithm for calculating vortex statistics, *Physics of Fluids*, *9*, 1988–1999.

Smith, W. H. F., and D. T. Sandwell (1997), Global sea floor topography from satellite altimetry and ship depth soundings, *Science*, *227*, 1956–1962.

Speich, S., B. Blanke, and G. Madec (2001), Warm and cold water paths of a O.G.C.M. thermohaline conveyor belt, *Geophys. Res. Lett.*, *28*(2), 311–314.

Speich, S., B. Blanke, P. de Vries, S. Drijfhout, K. Döös, A. Ganachaud, and R. Marsh (2002), Tasman leakage: A new route in the global ocean conveyor belt, *Geophys. Res. Lett.*, *29*(10), 1416, doi:10.1029/2001GL014586.

Treguier, A., O. Boebel, B. Barnier, and G. Madec (2003), Agulhas eddy fluxes in a $1/6^o$ Atlantic model, *Deep-Sea Res. II*, *50*, 119–139.

van Aken, H. M., A. K. van Veldhoven, C. Vetha, W. P. M. de Ruijter, P. J. van Leeuwen, S. S. Drijfhout, C. P. Whittled, and M. Rouault (2003), Observations of a young Agulhas ring, Astrid, during MARE in March 2000, *Deep-Sea Res. II*, *50*, 167–195.

van Ballegooyen, R. C., M. L. Gründlingh, and J. R. E. Lutjeharms (1994), Eddy fluxes of heat and salt from the southwest Indian Ocean into the southeast Atlantic Ocean: A case study, *J. Geophys. Res.*, *99*(C7), 14,053–14,070.

Wang, D. P. (1993), Model of frontogenesis: subduction and upwelling, *J. Mar. Res.*, *51*, 497–513.

Weijer, W., W. P. M. de Ruijter, H. A. Dijkstra, and P. J. van Leeuwen (1999), Impact of interbasin exchange on the Atlantic overturning circulation, *J. Phys. Oceanogr.*, *29*, 2266–2284.

Weiss, J. (1991), The dynamics of enstrophy transfer in two-dimensional hydrodynamics, *Physica D*, *48*, 273–294.

Wickerhauser, M. V. (1994), *Adapted Wavelet Analysis from Theory to Software*, xii + 486 pp., AK Peters, Ltd., Wellesley, Massachusetts.

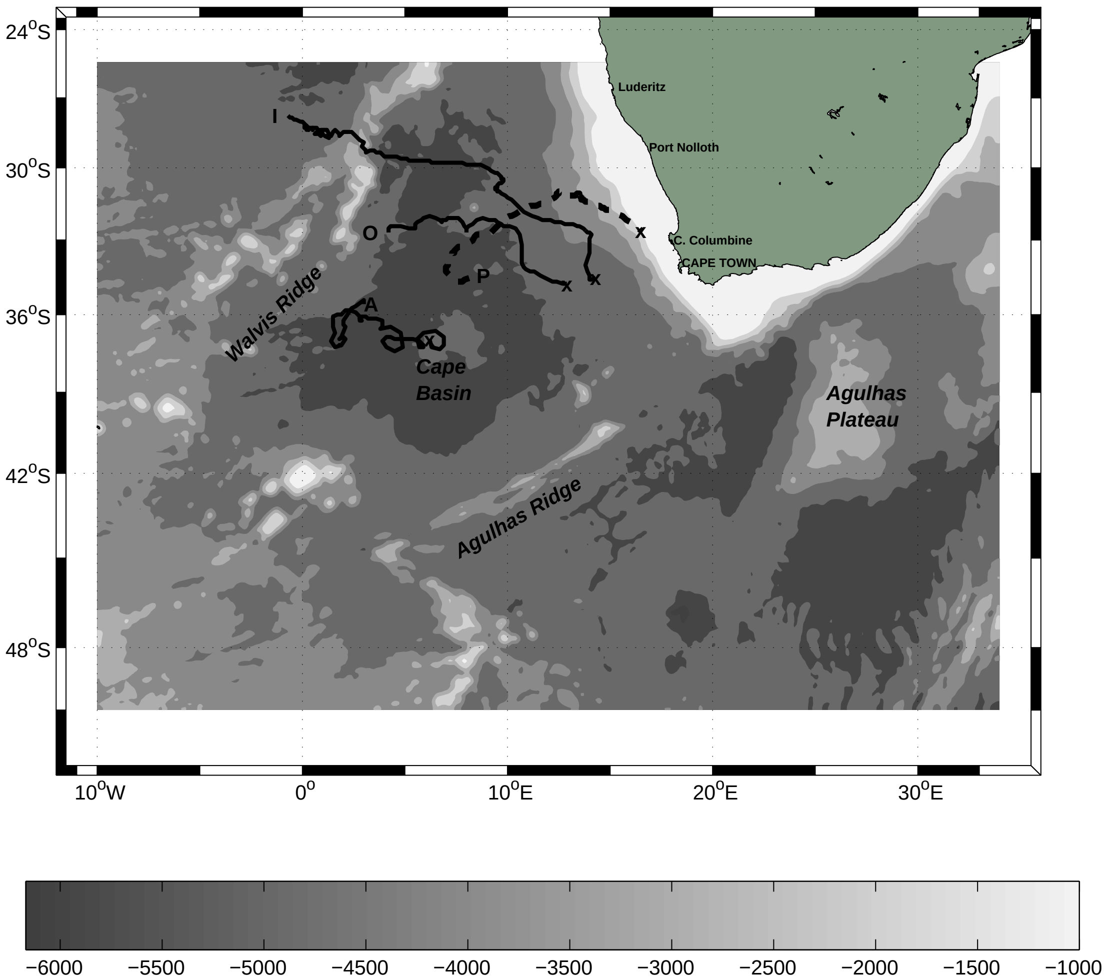

Figure 1. Model domain and bathymetry [m]. The trajectories of three anticyclones (solid lines) and one cyclone (dashed line) are drawn in black. Cross symbols and letters indicate the beginning and end of each trajectory, respectively. P=Panoramix, I=Idefix, O=Obelix, A=Asterix, see section 3 for nomenclature.

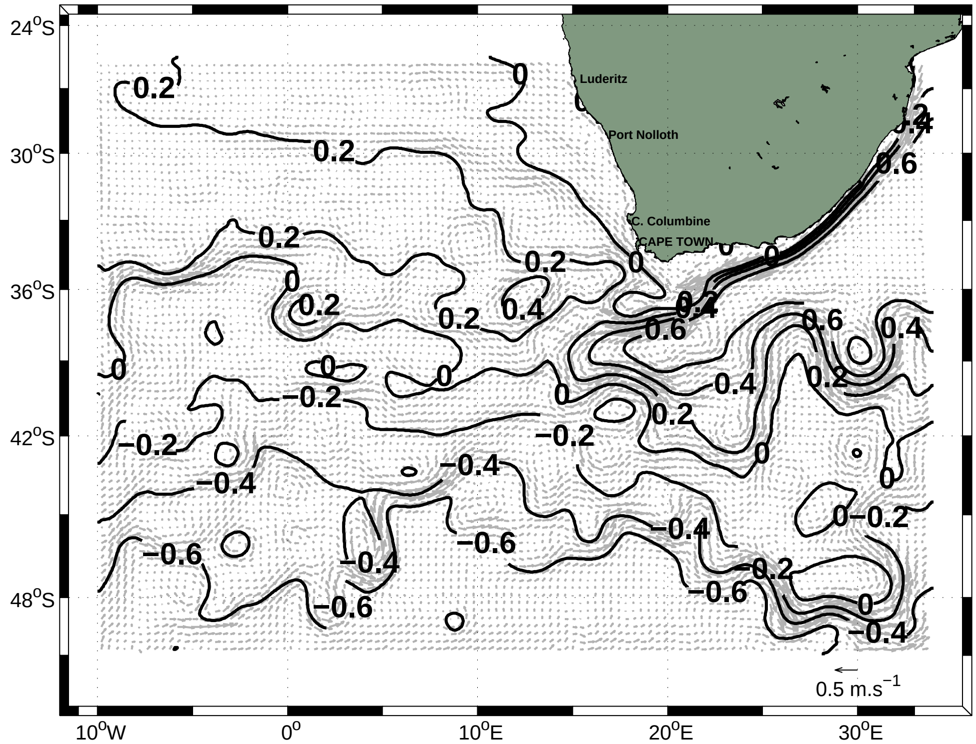

Figure 2. Model-climatology. Contour lines and arrows show the SSH anomaly [m] and barotropic current [m s^{-1}], respectively.

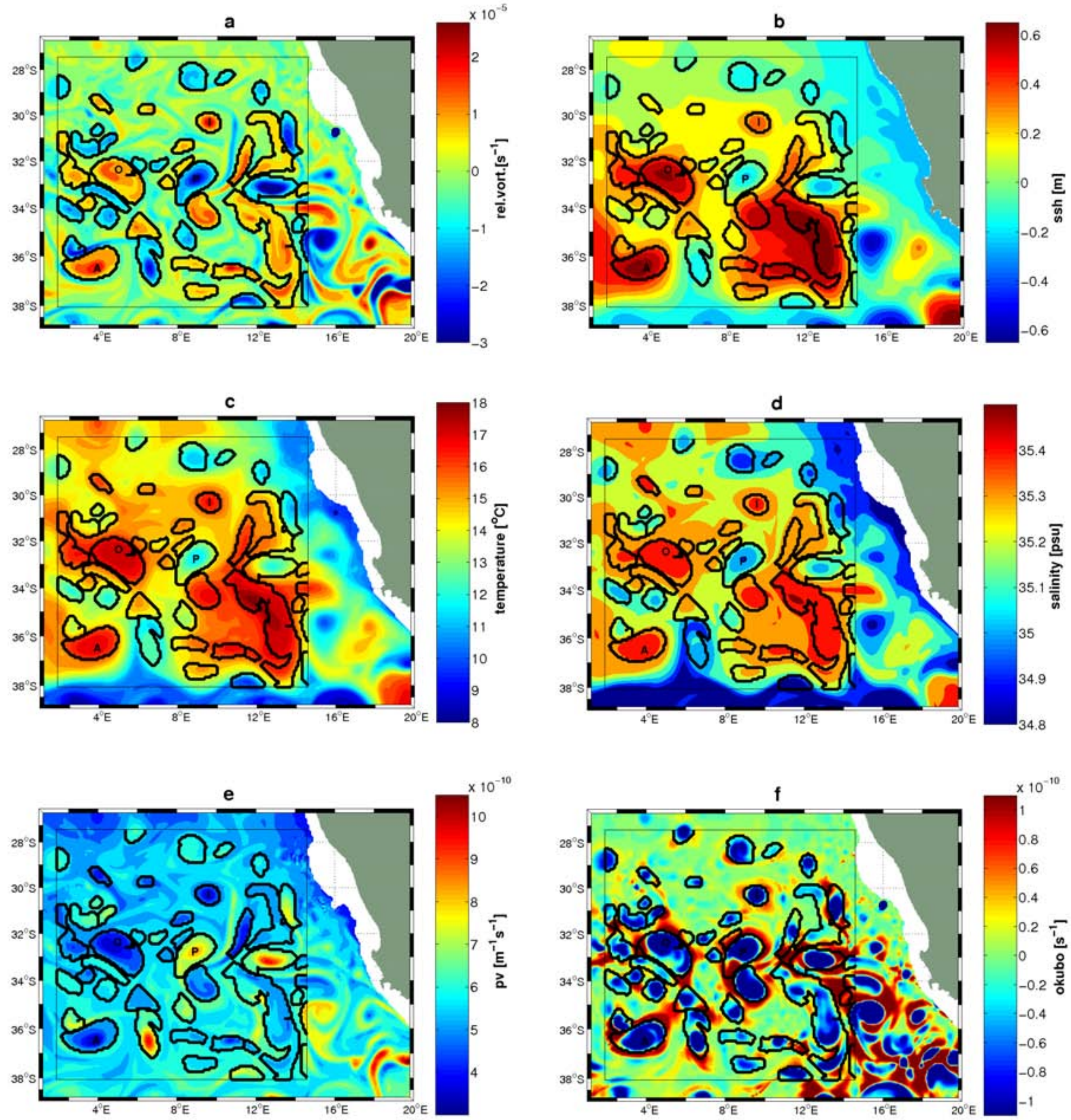

Figure 3. Wavelet analysis. Shaded colors represent (a) relative vorticity [s^{-1}], (b) SSH anomaly [m], (c) temperature [°C], (d) salinity [psu], (e) potential vorticity [$m^{-1}s^{-1}$] and (f) Okubo-Weiss criterion [s^{-1}]. All fields are calculated on day 11 / month 3 / year 7 and, except SSH, at depth -200 m. The black square shows the 256 × 256 gridpoint domain of the wavelet analysis applied on relative vorticity, and the identified eddies are contoured in black. Letters A, O, I and P indicate anticyclones Asterix, Obelix and Idefix and cyclone Panoramix, respectively.

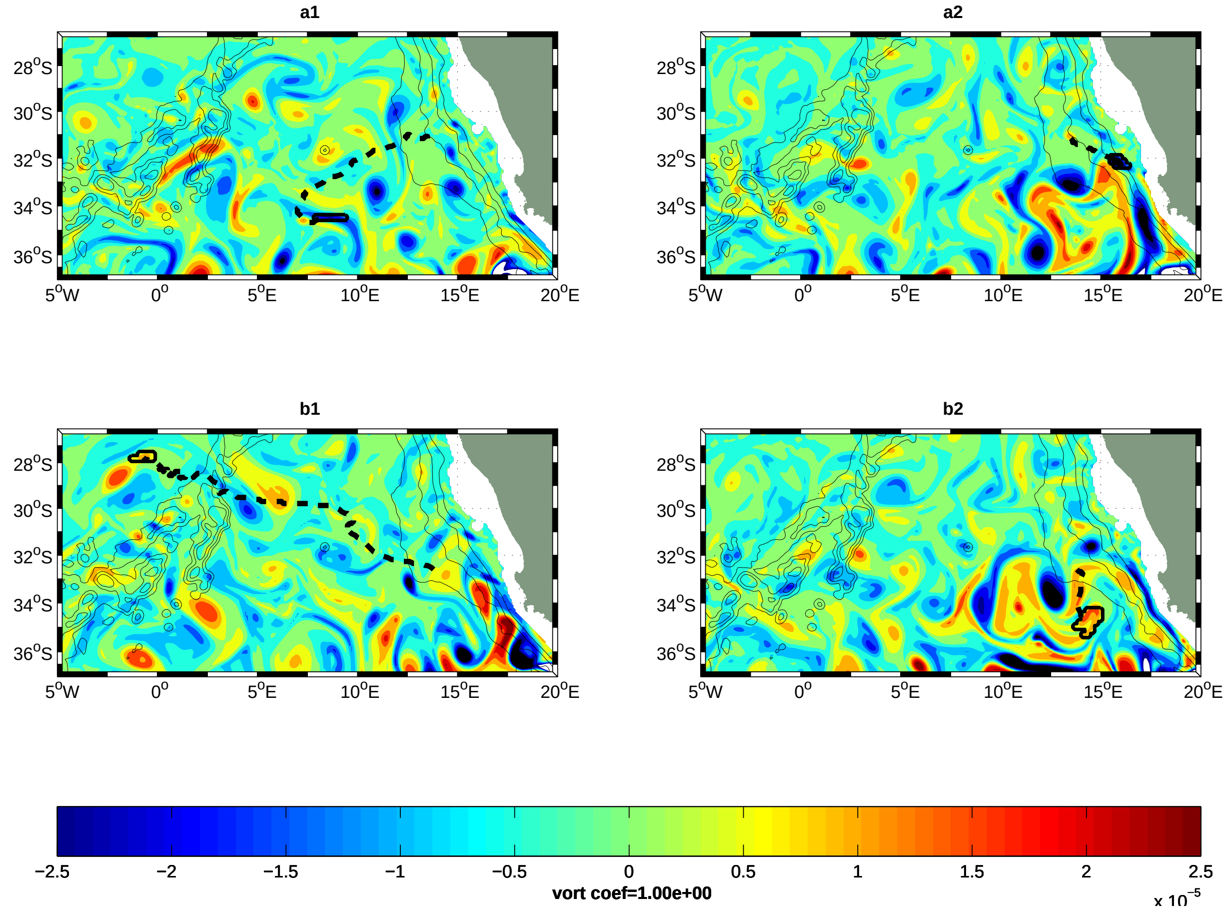

Figure 4. "Death"(left panels) and "birth"(right panels) of cyclone Panoramix (upper panels) and anticyclone Idefix (lower panels). Eddy patterns are shown by black and thick solid lines. Forward (left panels) and backward in time (right panels) trajectory segments are drawn with black and thick dashed lines. Bathymetry is shown in black and thin solid contours (-1000, -2000, -3000, -4000 m). Relative vorticity [s^{-1}] is shown in color at times (a1) day 14 / month 5 / year 7, (a2) 10/11/6, (b1) 11/10/7 and (b2) 3/12/6.

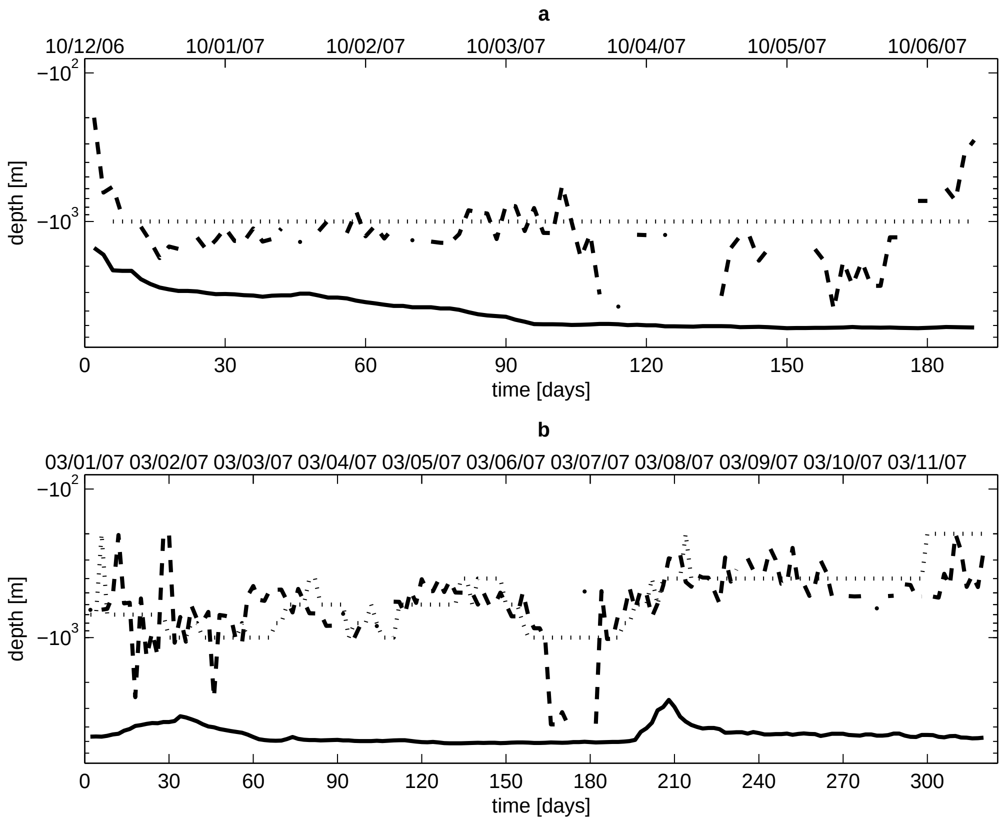

Figure 5. Vertical tracking. Time series of the deepest vertical tracking level, iz_L, reached by the wavelet analysis (dotted line), the maximum depth at which Flierl's criterion can be defined (dashed line) and bathymetry below the eddy center (solid line). For (a) cyclone Panoramix and (b) anticyclone Idefix.

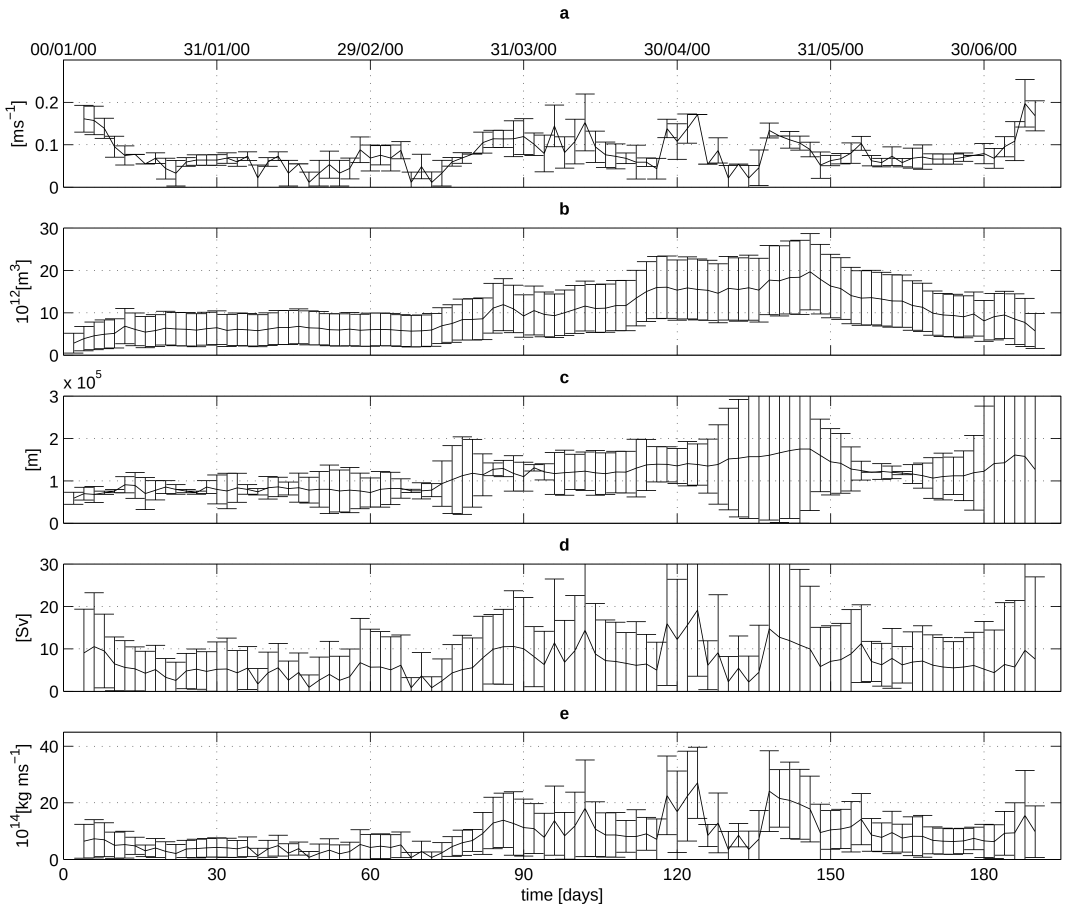

Figure 6. (a) Translational velocity, (b) volume, (c) diameter, (d) instantaneous transport and (e) instantaneous momentum of cyclone Panoramix.

.

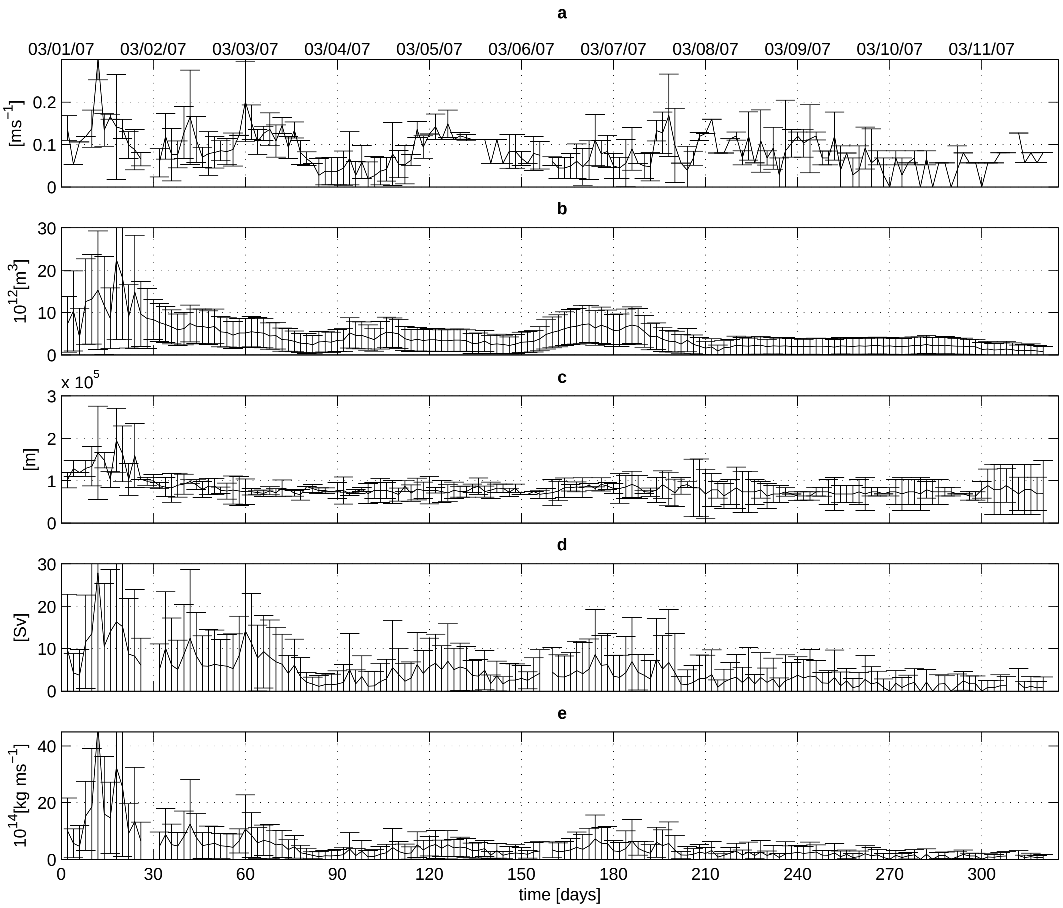

Figure 7. Same as Fig. 6, but for anticyclone Idefix.

.

eddy name	PANORAMIX	IDEFIX	OBELIX	ASTERIX
tracking duration [days]	190	320	110	150
$\overline{v}$ [ms^{-1}]	0.079	0.083	0.127	0.115
$\overline{V}$ 10^{12}[m^3]	10	4	14	12
$\overline{D}$ [km]	111	81	156	128
$\overline{Tinst}$ [Sv]	6.8	4.3	5.7	5.9
$\overline{Minst}$ 10^{14}[kg ms^{-1}]	8.2	4.0	5.3	6.1

Table 1. Time-averaged eddy parameters

.